# Palmitoylation regulates glutamate receptor distributions in postsynaptic densities through control of PSD95 conformation and orientation

Okunola Jeyifous[a,b,1], Eric I. Lin[a,b,1], Xiaobing Chen[b,c], Sarah E. Antinone[a], Ryan Mastro[a], Renaldo Drisdel[a], Thomas S. Reese[b,c,2], and William N. Green[a,b,2]

[a]Department of Neurobiology, University of Chicago, Chicago, IL 60637; [b]Marine Biological Laboratory, Woods Hole, MA 02543; and [c]Laboratory of Neurobiology, National Institute of Neurological Disorders and Stroke, National Institutes of Health, Bethesda, MD 20892

Contributed by Thomas S. Reese, October 23, 2016 (sent for review August 4, 2016; reviewed by Daniel Choquet and John Marshall)

**Postsynaptic density protein 95 (PSD95) and synapse-associated protein 97 (SAP97) are homologous scaffold proteins with different N-terminal domains, possessing either a palmitoylation site (PSD95) or an L27 domain (SAP97). Here, we measured PSD95 and SAP97 conformation in vitro and in postsynaptic densities (PSDs) using FRET and EM, and examined how conformation regulated interactions with AMPA-type and NMDA-type glutamate receptors (AMPARs/NMDARs). Palmitoylation of PSD95 changed its conformation from a compact to an extended configuration. PSD95 associated with AMPARs (via transmembrane AMPAR regulatory protein subunits) or NMDARs [via glutamate ionotropic receptor NMDA-type subunit 2B (GluN2B) subunits] only in its palmitoylated and extended conformation. In contrast, in its extended conformation, SAP97 associates with NMDARs, but not with AMPARs. Within PSDs, PSD95 and SAP97 were largely in the extended conformation, but had different orientations. PSD95 oriented perpendicular to the PSD membrane, with its palmitoylated, N-terminal domain at the membrane. SAP97 oriented parallel to the PSD membrane, likely as a dimer through interactions of its N-terminal L27 domain. Changing PSD95 palmitoylation in PSDs altered PSD95 and AMPAR levels but did not affect NMDAR levels. These results indicate that in PSDs, PSD95 palmitoylation, conformation, and its interactions are dynamic when associated with AMPARs and more stable when associated with NMDARs. Altogether, our results are consistent with differential regulation of PSD95 palmitoylation in PSDs resulting from the clustering of palmitoylating and depalmitoylating enzymes into AMPAR nanodomains segregated away from NMDAR nanodomains.**

palmitoylation | PSD95 | SAP97 | NMDA receptor | AMPA receptor

Postsynaptic densities (PSDs) at glutamatergic synapses organize and hold NMDA receptors (NMDARs), AMPA receptors (AMPARs), and other signaling molecules in place, apposed to sites of neurotransmitter release. Just below the PSD plasma membrane lies a latticework of vertical and parallel filaments that provides a structural scaffold to stabilize synaptic signaling molecules within PSDs (1, 2). Postsynaptic density protein 95 (PSD95) and synapse-associated protein 97 (SAP97) are members of a family of membrane-associated guanylate kinases (MAGUKs) (3). PSD95 is the most abundant scaffold protein in adult synapses, with ∼300 PSD95 molecules (2.3% of the mass of the PSD) in the average PSD, and is part of the lattice forming the core of the PSD (4). SAP97 is also a component of the PSD lattice. Estimates of its PSD copy numbers range from 90 SAP97 molecules per average PSD [0.9% of the mass of the PSD (4)] to lower values (5). As MAGUKs, PSD95 and SAP97 share a series of highly homologous protein-interacting domains but diverge at their N-terminal domains, which affects their trafficking into and out of the PSD, as well as interactions with AMPARs and NMDARs (3, 6, 7). The SAP97β-isoform, like almost all SAP97 molecules, contains an N-terminal L27 domain that interacts with other L27 domain-containing proteins, particularly with a different MAGUK, CASK (8). Most PSD95 molecules, like the PSD95α-isoform, contain, instead of an L27 domain, an N-terminal protein palmitoylation domain, which is required for PSD95 synaptic targeting and retention in the PSD (9–11).

The insoluble nature of isolated PSD fractions has prevented detailed biochemical characterization of interactions between MAGUKs (e.g., PSD95 and SAP97) and glutamate receptors (NMDARs and AMPARs) within PSDs, whereas in vitro binding analysis of these interactions has provided significant insights. The first two PDZ domains of PSD95 and SAP97 bind the C-terminal 5 to 7 aa of different AMPAR and NMDAR subunits (12, 13). PSD95 and SAP97 can both bind the NMDAR, GluN2 subunits, but also bind to different subunits. SAP97 can bind directly to AMPARs via the C terminus of GluA1 subunits (14). PSD95 does not bind to GluA1 subunits and, instead, interacts with the C terminus of AMPAR auxiliary subunits, transmembrane AMPAR regulatory proteins (TARPs), such as Stargazin (15). It has been proposed that when integrated into PSDs, PSD95 serves as a dynamic "slot" that binds AMPARs at the PSD periphery as they enter and exit PSDs (16–18).

Although it had been assumed that NMDARs and AMPARs are homogeneously distributed within PSDs, mounting evidence suggests that assumption is not true. Early immuno-EM studies showed a differential distribution of NMDARs and AMARs at the PSDs in

## Significance

**Synaptic AMPA-type and NMDA-type glutamate receptors (AMPARs and NMDARs) have different dynamic characteristics critical for synaptic plasticity. We find that the posttranslational modification, palmitoylation, changes the conformation of postsynaptic density protein 95 (PSD95), a major synaptic scaffold, promoting interactions with AMPARs and NMDARs. In synapses, we measured the conformation and orientation of palmitoylated PSD95 relative to the scaffold, synapse-associated protein 97 (SAP97), and found that changing PSD95 palmitoylation altered PSD95 and AMPAR levels, but not NMDAR levels. We conclude that palmitoylation regulates PSD95 conformation and retention of AMPAR and NMDARs at synapses. Differences in PSD95 palmitoylation appear to occur when AMPARs and NMDARs are in separate synaptic domains, likely contributing to differences in AMPAR and NMDAR dynamics in synapses.**

Author contributions: O.J., E.I.L., X.C., T.S.R., and W.N.G. designed research; O.J., E.I.L., X.C., S.E.A., R.M., and R.D. performed research; E.I.L. contributed new reagents/analytic tools; O.J., E.I.L., X.C., S.E.A., and R.M. analyzed data; and O.J., E.I.L., X.C., T.S.R., and W.N.G. wrote the paper.

Reviewers: D.C., Université de Bordeaux; and J.M., Brown University.

The authors declare no conflict of interest.

Freely available online through the PNAS open access option.

[1]O.J. and E.I.L. contributed equally to this work.

[2]To whom correspondence may be addressed. Email: treese@mbl.edu or wgreen@uchicago.edu.

This article contains supporting information online at www.pnas.org/lookup/suppl/doi:10.1073/pnas.1612963113/-/DCSupplemental.

hippocampal and cortical synapses (19, 20). New studies using superresolution light microscopy observed that AMPARs (21, 22) and palmitoylated PSD95 (22, 23) within PSDs were clustered in nanodomains. Using EM tomography, Chen et al. (1, 2) found NMDAR clusters were separate from AMPARs. The NMDAR nanodomain contained NMDAR–PSD95 complexes in a 1:2 stoichiometry, whereas other PSD regions with AMPARs contained AMPAR–PSD95 complexes in a 1:1 stoichiometry. PSD95-like vertical filaments interacted directly with both NMDAR and AMPAR complexes in PSDs (2), suggesting that there are differences in how PSD95 associates with the two glutamate receptor subtypes. When PSD95 was acutely knocked down, AMPAR nanodomains were lost, whereas NMDAR nanodomains were relatively preserved in PSDs (1). This result is consistent with NMDAR nanodomains being more stable than AMPAR nanodomains, and also consistent with the idea that there are important differences in how PSD95 associates with NMDARs and AMPARs at the PSD. Studies assaying the recycling of AMPARs and NMDARs at mature glutamatergic synapses have also found that, compared with AMPARs, NMDARs are more stable in PSDs (24–26). The presence of separate domains in PSDs, together with differences in how PSD95 interacts with AMPARs and NMDARs, suggests that PSD95 has an important role as a scaffold in forming and maintaining separate AMPAR and NMDAR nanodomains.

Previously, we found that SAP97 binding to AMPAR and NMDAR subunits was dependent on conformational change from a "compact" to "extended" conformation (27). Here, we assay PSD95 conformation and demonstrate that it changes from a compact to extended conformation regulated by its palmitoylation. Palmitoylation is a reversible posttranslational modification in which the fatty acid, palmitate, is attached to cysteine residues at the N terminus of PSD95 (28). It provides soluble proteins, such as PSD95, with an anchor to associate with membranes. PSD95 bound directly with NMDAR and AMPAR subunits only in its palmitoylated and extended conformation, and the binding was absent in the compact conformation. PSD95 and SAP97 were largely in the extended conformation at PSDs, and in the compact conformation outside of synapses. However, PSD95 was oriented perpendicular to the PSD plane, with its palmitoylated N terminus at the membrane, whereas SAP97 was oriented parallel to the PSD plane. Increasing PSD95 palmitoylation in PSDs increased PSD95 and AMPAR levels but did not affect NMDAR levels. Thus, in PSDs, PSD95 palmitoylation and conformation are more dynamic when associated with AMPARs and more stable when associated with NMDARs. Evidence of separate AMPAR and NMDAR nanodomains from other studies suggests partitioning of palmitoylating and depalmitoylating enzymes into AMPAR nanodomains separate from NMDAR nanodomains. We propose that regulation of PSD95 and SAP97 conformation changes, and their dynamics in PSDs, results in different interactions with NMDARs and AMPARs, thereby segregating and clustering the receptors in separate nanodomains more dynamic for AMPARs and more stable for NMDARs.

## Results

**Palmitoylation and Depalmitoylation Regulate PSD95 Conformation.** To assay for conformational changes in the predominant PSD95 splice variant, PSD95α (referred to here as PSD95), we generated a PSD95 FRET construct (Ch-PSD95-V; Fig. 1*A*). Ch-PSD95-V was created by adding the mCherry and Venus fluorescent proteins to the N and C termini of PSD95, respectively. The mCherry sequence was inserted downstream of the palmitoylation sites (3,5 Cys) (29) (Fig. 1*A*), which allowed palmitoylation of Ch-PSD95-V (Fig. S1). We also mutated the two palmitoylated cysteine residues at the N terminus to serines, as previously described (29), to make a palmitoylation-deficient version of the PSD95 FRET sensor (C3,5S-Ch-PSD95-V; Fig. 1*A*). The distribution of the PSD95 FRET construct in cultured rat hippocampal neurons was indistinguishable from the distribution of native PSD95 or PSD95 with GFP attached to the C terminus (e.g., see Fig. 3*A* and Fig. S1). In contrast to the intact Ch-PSD95-V, C3,5S-Ch-PSD95-V trafficking to spines in cultured hippocampal neurons was highly reduced (Fig. S1). These results are consistent with previous findings that PSD95 is palmitoylated to traffic into synapses (11).

Ch-PSD95-V FRET efficiency (Fig. 1*B*) was determined using an acceptor photobleaching protocol (Fig. S2). The protocol measured increases in Venus fluorescence after successive photobleaching of mCherry. The FRET efficiency, 17.7%, was calculated from the fit to the values of the fluorescence changes with successive photobleaching. Importantly, no FRET was observed when the FRET pairs were attached separately to the N or C terminus of PSD95 (Ch-PSD95 and PSD95-Venus) and coexpressed in HEK293 cells (Fig. S2). The FRET measured using Ch-PSD95-V is therefore intramolecular and does not result from intermolecular FRET between two or more Ch-PSD95-V molecules. Using a FRET sensor of SAP97 conformation with the same FRET pair (Ch-SAP97-V), we previously found that SAP97 conformation changes from a compact conformation to an extended conformation when the protein CASK binds to its N-terminal domain (27). The relatively high FRET efficiency measurement of 17.7% is consistent with interacting FRET pairs of N and C termini. Therefore, PSD95 is predominantly in the compact conformation, as shown by EM of recombinant PSD95 molecules (30). If palmitoylation of PSD95 changes its conformation from a compact conformation to an extended conformation, similar to how CASK affects SAP97 conformation, we would expect a decrease in FRET efficiency of Ch-PSD95-V when it is palmitoylated. We would therefore expect the C3,5S-Ch-PSD95-V FRET sensor, which cannot be palmitoylated, to have the highest FRET efficiency. We observed a small, but not statistically significant, increase (17.7% vs. 20.6%) comparing FRET efficiencies of Ch-PSD95-V with C3,5S-Ch-PSD95-V (Fig. 1*B*, *Top* and Fig. S3, *Top*). The small change in FRET efficiency suggests that either the level of Ch-PSD95-V palmitoylation is relatively low or that palmitoylation has little effect on PSD95 conformation.

To assess further how palmitoylation affects PSD95 conformation, we altered conditions in the HEK cells to increase PSD95 palmitoylation. First, we coexpressed zinc finger DHHC-type containing 15 (DHHC15), a palmitoyl-acyl transferase (PAT), which increased its palmitoylation and redistributed PSD95 into perinuclear clusters with DHHC15 when expressed in heterologous cells with PSD95 (31). When coexpressed, perinuclear clusters of Ch-PSD95-V that colocalized with DHHC15 were observed (Fig. S3). The clustering was not observed when C3,5S-Ch-PSD95-V replaced Ch-PSD95-V (Fig. S3). Thus, the clusters are consistent with an interaction between DHHC15 and Ch-PSD95-V that increases Ch-PSD95-V palmitoylation. Ch-PSD95-V FRET efficiency with DHHC15 coexpression was significantly reduced from 18.0% to 9.9%, whereas the FRET efficiency of C3,5S-Ch-PSD95-V coexpressed with DHHC15 did not change (Fig. 1*B*).

Next, we coexpressed Ch-PSD95-V with a different PAT, DHHC2. DHHC2 differs from other PATs that can palmitoylate PSD95, such as DHHC15 and DHHC3, in that it is trafficked to the neuronal plasma membrane at PSDs, and appears to be the native PAT that palmitoylates PSD95 at PSDs (9, 23). Ch-PSD95-V redistributed into even larger perinuclear clusters (Fig. S3) when coexpressed with DHHC2. The Ch-PSD95-V FRET efficiency in the clusters with DHHC2 coexpression was further reduced, from 18.0% to 4%, compared with the reduction to 9.9% observed with DHHC15 coexpression (Fig. 1*C*). As an alternative to coexpression with DHHC proteins, we used palmostatin B to inhibit the palmitoyl-thioesterase (PPT) that depalmitoylates PSD95, and thereby to increase its palmitoylation. Treatment of cells expressing Ch-PSD95-V with palmostatin B again caused Ch-PSD95-V redistribution into perinuclear clusters similar in size to the clusters observed with DHHC2 coexpression (Fig. S3), consistent with Ch-PSD95-V clustering caused by its palmitoylation. Ch-PSD95-V FRET efficiency decreased from 18.0% to 5% under this condition

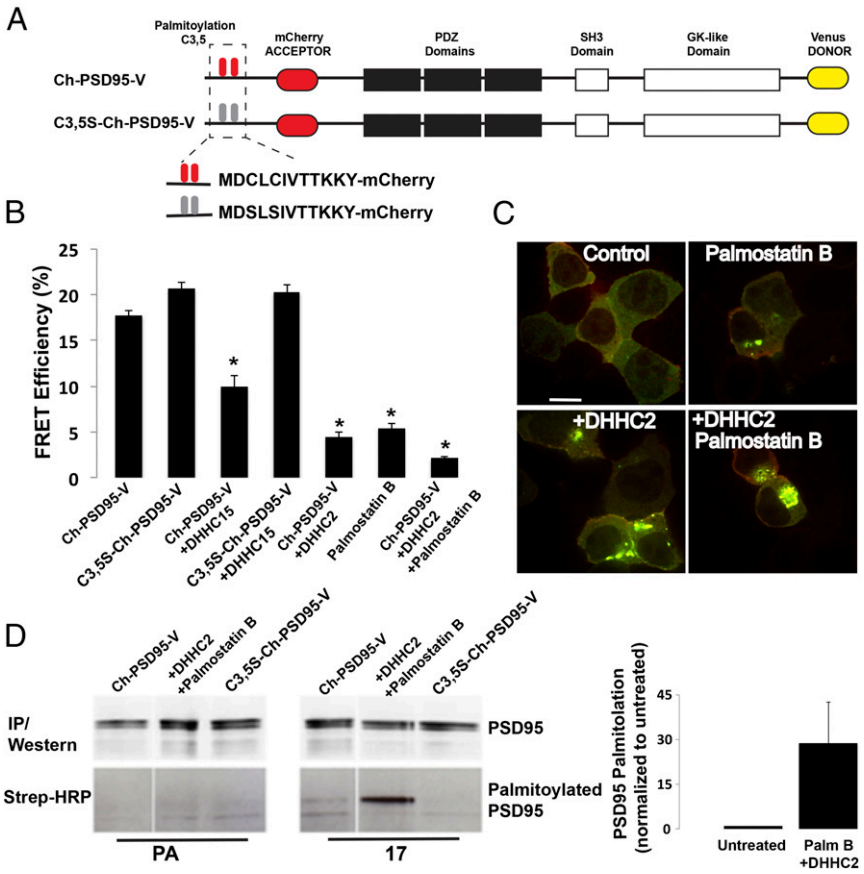


**Fig. 1.** Palmitoylation of PSD95 triggers a change in PSD95 conformation. (*A*) Schematic of PSD95 (Ch-PSD95-V) and mutated PSD95 (C3,5S-Ch-PSD95-V) FRET sensor constructs. (*B*) FRET efficiency values for Ch-PSD95-V with changes in palmitoylation. FRET measurements were made in regions of interest in example cells shown in Fig. S3. Data are shown as mean ± SEM ($n$ = 12–30 cells per condition; *$P < 0.0001$ relative to Ch-PSD95-V). (*C*) As an additional assay of the changes in PSD95 palmitoylation observed above, we used colocalization with PF11-GFP, a conformation-specific intrabody for palmitoylated PSD95. Representative images of HEK cells expressing PF11-GFP and PSD95 alone (*Top Left*), with DHHC2 (*Bottom Left*), with palmostatin B treatment (*Top Right*), or with palmostatin B treatment and DHHC2 expression (*Bottom Right*). Increased aggregation and colocalization with PF11-GFP is correlative with an increase in PSD95 palmitoylation. PSD95 alone is not highly palmitoylated (diffuse fluorescence and lack of colocalization with PF11-GFP) compared with its palmitoylation in the presence of DHHC2 and palmostatin B (coaggregation and colocalization with PF11-GFP). (Scale bar: 10 μm.) (*D*) Click chemistry palmitoylation assay was used to compare the level of Ch-PSD95-V palmitoylation under different conditions. HEK cells transiently expressing Ch-PSD95-V alone or with Myc-DHHC2 and palmostatin B treatment were labeled with 17-octadecynoic acid (17-ODYA). Ch-PSD95-V was immunoprecipitated and treated with biotin-azide under click chemistry reaction conditions, and subsequently analyzed by Western blotting with anti-PSD95 antibody (*Top*) and streptavidin (*Bottom*). The space after the first lane is due to cropping of lanes unrelated to the present analysis. PSD95 alone is not highly palmitoylated. In the bar graph, quantification of the normalized band intensities (ratio of streptavidin signal to PSD95 protein) indicates that Ch-PSD95-V palmitoylation increases 30-fold in the presence of DHHC2 and palmostatin B ($n$ = 4 experiments). IP, immunoprecipitation.

(Fig. 1*B*). For a final condition, we coexpressed DHHC2 with Ch-PSD95-V, and the cells were also treated with palmostatin B. The largest Ch-PSD95-V perinuclear clusters were observed under these conditions, suggesting that Ch-PSD95-V palmitoylation is highest under these conditions (Fig. S3), and the FRET efficiency decreased from 18.0% to 2% (Fig. 1*B*). Altogether, our results are consistent with palmitoylation of Ch-PSD95-V causing a change in its conformation from a compact to extended conformation.

To test directly whether the PSD95 in the perinuclear clusters was palmitoylated, we obtained an "intrabody," PF11, a recombinant IgG fragment that specifically recognizes and binds to palmitoylated PSD95 but not to depalmitoylated PSD95 (23). PF11, tagged with GFP (PF11-GFP), was coexpressed with PSD95. In the PSD95-alone condition, PF11 and PSD95 were almost always evenly distributed throughout the cell cytoplasm whether expressed together or alone. When the PSD95 perinuclear clusters formed with coexpression of DHHC2 and/or palmostatin B treatment (Fig. 1*C*), PF11-GFP colocalized predominantly in the clusters, demonstrating the presence of palmitoylated PSD95. The conditions that increased PSD95 clustering, and presumably its palmitoylation (coexpression of DHHC2 and/or palmostatin B), also increased PF11-GFP clustering and colocalization. No clustering of PF11-GFP was observed without coexpression of PSD95. Together, our data demonstrate that the clustering of PSD95 is caused by its palmitoylation and that the size and extent of the clustering correlate with the degree to which PSD95 is palmitoylated.

Using click chemistry methods (32) to quantitate changes in Ch-PSD95-V palmitoylation, we estimated the change in PSD95 palmitoylation with the addition of DHHC2 and palmostatin B treatment in the cells. The results were somewhat variable, but indicated that the DHHC2 enzyme, together with palmostatin B treatment, resulted in an increase in PSD95 palmitoylation of ~30-fold (Fig. 1*D*).

**PSD95 Palmitoylation Is Required for Its Associations with AMPARs and NMDARs.** We performed additional experiments in HEK cells to examine how palmitoylation and changes in PSD95 conformation might regulate its interactions with AMPARs and NMDARs. PSD95 does not associate directly with AMPAR subunits. Instead, PSD95 associates indirectly with AMPARs through a direct interaction with

their auxiliary TARP subunits. PSD95–TARP interactions depend on the TARP PDZ-binding domain at its C terminus (33). In HEK cells, we examined whether palmitoylation regulates the interaction between PSD95 and the TARP Stargazin. When Ch-PSD95-V was expressed with AMPAR GluA1 subunits and Stargazin, we observed it in clusters with GluA1 and Stargazin at the cell surface and at intracellular sites (Fig. 2*A*). We did not find any PSD95-GluA1-Stargazin clusters when PSD95 was replaced by C3,5S-PSD95 (Fig. 2*A*). PSD95 also binds directly to NMDAR, GluN2 subunits. Consistent with this property, we observed strong colocalization between GluN2B-containing NMDARs and PSD95 when coexpressed in HEK293 cells in small clusters at the cell surface and at intracellular sites as previously reported (34) (Fig. 2*B*). Again, we did not find any PSD95-NMDAR clusters when PSD95 was replaced by C3,5S-PSD95 (Fig. 2*B*). Furthermore, PSD95-NMDAR clusters disappeared when HEK293 cells were treated with 2-bromopalmitate (2-BP), an inhibitor of palmitoylation (Fig. S4*A*).

To examine the conformation of PSD95 where interactions with the different receptor subunits occur, we measured Ch-PSD95-V FRET efficiency in the PSD95 clusters colocalized with glutamate receptor subunits (Fig. 2*C*). In puncta where Ch-PSD95-V and GluN2B-containing NMDARs in HEK293 cells colocalized, the Ch-PSD95-V FRET efficiency was reduced from 18.0% to 1.8% (Fig. 2*C*), significantly lower than when coexpressed with DHHC15 or DHHC2, or when treated with palmostatin B (Fig. 1). These conditions were similar to conditions where PSD95 appears to be most highly palmitoylated, that is, when in puncta coexpressed with DHHC2 and treated with palmostatin B. Similarly, when in puncta

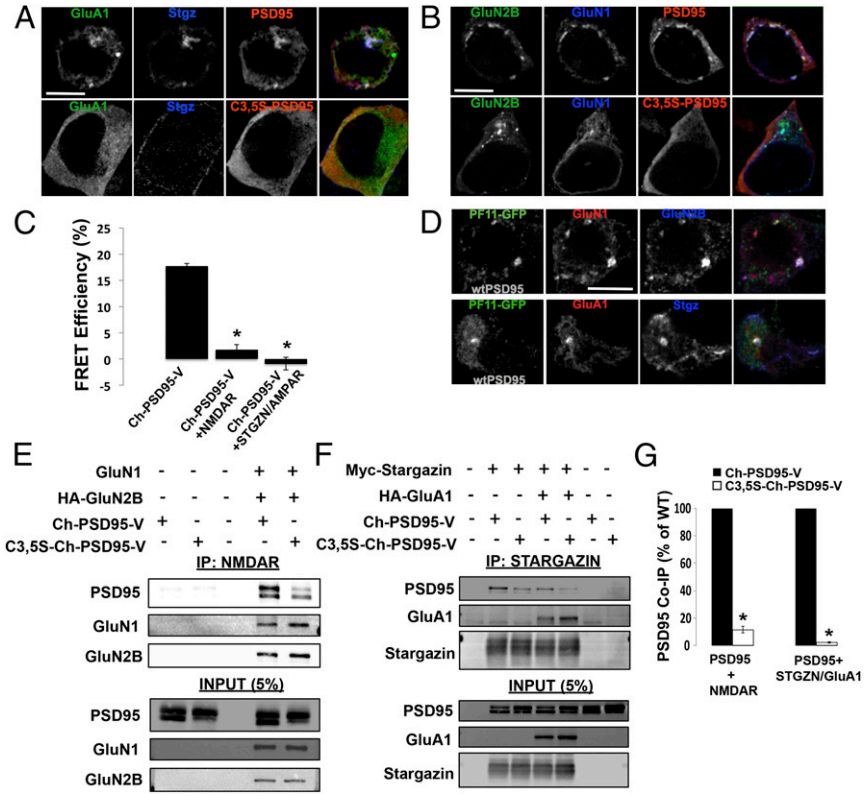


**Fig. 2.** Palmitoylation of PSD95 regulates interactions with AMPARs and NMDARs. (*A*) Immunolocalization of HA-Stargazin, GFP-GluA1, and untagged wild-type (wt) PSD95 or C3,5S-PSD95 in HEK293 cells. (*Top*) PSD95, HA-Stargazin, and GFP-GluA1 AMPAR subunits transfected in HEK293 cells. (*Bottom*) C3,5S-PSD95 replaced PSD95. In both sets of images, PSD95 or C3,5S-PSD95 was detected with anti-PSD95 antibodies, and with anti-HA antibodies for Stargazin. (Scale bar: 10 μm.) (*B*) Immunolocalization of NMDARs (GFP-GluN2B and Flag-GluN1) and untagged PSD95 or C3,5S-PSD95 in HEK293 cells. (*Top*) PSD95, GFP-GluN2B, and Flag-GluN1 NMDAR subunits transfected in HEK293 cells. (*Bottom*) C3,5S-PSD95 replaced PSD95. In both sets of images, PSD95 or C3,5S-PSD95 was detected with anti-PSD95 antibodies, and with anti-Flag antibodies for GluN1. (Scale bar: 10 μm.) (*C*) Ch-PSD95-V FRET analysis to test for conformational changes that occur with interactions with NMDARs and AMPARs in HEK293 cells. Cells were transfected with Ch-PSD95-V and NMDARs, consisting of HA-GluN2B/Flag-GluN1, or with AMPARs, consisting of Myc-Stargazin/HA-GluA1. (*D*) Palmitoylated PSD95 specifically colocalized in puncta with NMDARs and AMPARs in HEK293 cells. Cells were transfected with PF11-GFP, the conformation-specific intrabody for palmitoylated PSD95, untagged wtPSD95, and either Flag-GluN1 plus HA-GluN2B (NMDARs, *Top*) or mCherry-GluA1 plus HA-Stargazin (AMPARs, *Bottom*). Flag-GluN1, HA-GluN2B, and HA-Stargazin were detected with anti-Flag and anti-HA antibodies. (Scale bar: 10 μm.) (*E*) Loss of PSD95 palmitoylation sites disrupts interactions between PSD95 and NMDARs. PSD95–NMDAR interactions were assayed by co-IP and Western blots. A representative Western blot shows the levels of Ch-PSD95-V that coimmunoprecipitated with GluN2B subunits. Cell lysates prepared from HEK293 cells expressing NMDARs (Flag-GluN1 and HA-GluN2B) were mixed with separate lysates from cells expressing Ch-PSD95-V or C3,5S-Ch-PSD95-V. IPs were performed with anti-HA antibodies specific for GluN2B, and anti-PSD95 and anti-HA antibodies were used to blot. (*F*) Loss of PSD95 palmitoylation sites disrupts interactions between PSD95 and AMPARs containing Stargazin. A representative Western blot displays the levels of Ch-PSD95-V that coimmunoprecipitated with Stargazin subunits alone, or with Stargazin and GluA1 subunits. Cell lysates prepared from HEK293 cells expressing Stargazin-containing AMPARs (Myc-Stargazin and HA-GluA1) or Stargazin alone (Myc-Stargazin) were mixed with separate lysates from cells expressing Ch-PSD95-V or C3,5S-Ch-PSD95-V. IPs were performed with anti-Myc antibodies specific for Stargazin, and anti-PSD95 and anti-HA antibodies were used to blot. (*G*, *Left*) Quantification of band intensities for Ch-PSD95-V and C3,5S-Ch-PSD95-V that coprecipitated with NMDAR subunits from four separate Western blots. Band intensities are plotted as the percentage of wild-type (WT) PSD95, with Ch-PSD95-V set at 100%. The mean value for C3,5S-Ch-PSD95-V band intensities was 11.6 ± 2.3% (SEM), with $*P < 0.001$. (*G*, *Right*) Quantification of band intensities for Ch-PSD95-V and C3,5S-Ch-PSD95-V that coprecipitated with AMPAR subunits from four separate Western blots. Band intensities are plotted as the percent of WT PSD95, with Ch-PSD95-V set at 100%. The mean value for C3,5S-Ch-PSD95-V band intensities was 2.23 ± 0.5% (SEM), with $*P < 0.001$.

or clusters where Ch-PSD95-V and Stargazin-containing AMPARs colocalized, the Ch-PSD95-V FRET efficiency was reduced from 18.0% to –0.9% (Fig. 2*C*). At such low FRET efficiencies, we found that Ch-PSD95-V is both in an extended conformation and highly palmitoylated (Fig. 1). The low FRET efficiencies at clusters where PSD95 colocalizes with AMPARs or NMDARs thus suggest that the interactions between PSD95 and AMPARs and NMDARs are regulated by PSD95 palmitoylation, parallel to its changes in conformation.

To determine if the PSD95 localized to clusters containing AMPARs or NMDARs represents a palmitoylated pool, we used colocalization with the PF11 intrabody as a visual assay (Fig. 2*D*). PF11-GFP, which specifically recognizes palmitoylated PSD95, but not depalmitoylated PSD95 (23), was coexpressed with wild-type PSD95 and either GluN2B-containing NMDARs or Stargazin-containing AMPARs in HEK293 cells. PF11-GFP colocalized with NMDAR subunits, demonstrating the presence of palmitoylated PSD95 in PSD95-NMDAR clusters (Fig. 2*D*). Similarly, we observed colocalization in intracellular clusters between PF11-GFP and Stargazin-containing AMPARs (Fig. 2*D*). These data provide further evidence that PSD95 associated with either receptor subtype is specifically palmitoylated.

To test directly whether palmitoylation of PSD95 regulates the associations between PSD95 and NMDARs or AMPARs, we performed a series of coimmunoprecipitation experiments. Different combinations of PSD95 and NMDAR or AMPAR subunits expressed in HEK293 cells were used to compare results for PSD95 and C3,5S-PSD95, which cannot be palmitoylated. Detailed coimmunoprecipitation experiments were first performed for PSD95 or C3,5S-PSD95, and for GluN1 and/or GluN2B subunits. Surprisingly, we observed the same levels of coimmunoprecipitation between PSD95 and NMDAR subunits whether PSD95 was coexpressed with the NMDAR subunits in the same cells before solubilization or if the two components were expressed in a separate set of cells and the lysates were mixed before coimmunoprecipitations were performed (Fig. S4 *B–G*). Similar results with coimmunoprecipitations were obtained with PSD95 when it was expressed alone in HEK cells and the solute mixed with either the solute of cells expressing GluN2B alone or together with GluN1.

When palmitoylation-deficient C3,5S-PSD95 was substituted for PSD95, we no longer observed colocalization between PSD95 and NMDARs in HEK293 cells (Fig. 2*B*) nor could we coimmunoprecipitate C3,5S-PSD95 with GluN2B or with GluN2B-containing NMDARs (Fig. 2 *E* and *G* and Fig. S4 *B* and *C*). Similar results were obtained in a different study using GluN2A substituted for GluN2B (35). Thus, the association between PSD95 and NMDARs requires PSD95 N-terminal palmitoylation. We further tested this property using the palmitoylation inhibitor, 2-BP, which disrupted PSD95 coimmunoprecipitation with NMDAR subunits (Fig. S4) and prevented GluN2B-containing NMDARs from colocalizing with PSD95 (Fig. S4). We found a similar requirement for PSD95 N-terminal palmitoylation and its association with the TARP, Stargazin, associated with the AMPAR subunit GluA1 (Fig. 2 *F* and *G*). We observed a 33% decrease in the amount of PSD95 that immunoprecipitated with Stargazin alone versus Stargazin complexed with GluA1 (Fig. S5). This discrepancy is likely due to differences in the stoichiometry of PSD95 in the complexes formed with Stargazin alone versus Stargazin and GluA1. Importantly, both the Stargazin and Stargazin–GluA1 complexes coprecipitate much more with PSD95 possessing intact palmitoylation sites than with C3,5S-PSD95 lacking its palmitoylation sites. We conclude that PSD95 must be palmitoylated to stabilize interactions with NMDARs through its GluN2B subunit and with AMPARs through TARPs.

**PSD95 and SAP97 Have Similar Conformations but Different Orientations in PSDs.** PSD95 is highly palmitoylated in PSDs (11) and appears to be primarily oriented in an extended conformation perpendicular to the plane of the postsynaptic membrane (2). When expressed in cultured hippocampal neurons, Ch-PSD95-V, but not C3,5S-Ch-PSD95-V, was observed at PSDs as assayed by costaining with presynaptic Bassoon (Fig. 3*A* and Fig. S1). When FRET measurements were performed on Ch-PSD95-V outside of synapses, the FRET efficiency was high, 17.9% (Fig. 3*B*), identical to what was measured in HEK293 cells (Fig. 1*B*). For Ch-PSD95-V puncta at synapses, the FRET efficiency was low, 4.5% (Fig. 3*B*), very similar to the values obtained for Ch-PSD95-V in HEK293 cells in puncta formed when coexpressed with DHHC2 or when treated with palmostatin B (Fig. 1*B*). However, the FRET efficiency of the Ch-PSD95-V synaptic puncta was significantly higher than the values obtained when Ch-PSD95-V colocalized with Stargazin-containing AMPARs or GluN2B-containing NMDARs in HEK cells (Fig. 2*C*). The Ch-PSD95-V FRET efficiency outside of synapses indicates that nonsynaptic PSD95α is mostly in the compact conformation, and is likely not palmitoylated. At synapses, largely integrated in PSDs, the Ch-PSD95-V FRET efficiency indicates that most, but not all, of PSD95 is in the extended conformation and palmitoylated.

Using a FRET sensor of SAP97 conformation with the same FRET pair (Ch-SAP97-V), measurements of synaptic and extrasynaptic SAP97 conformations were obtained (Fig. 3*B*). When expressed in cultured hippocampal neurons, Ch-SAP97-V at PSDs was marked by costaining with presynaptic Bassoon (Fig. 3*A*). When FRET measurements were performed on Ch-SAP97-V outside of synapses, the FRET efficiency was high, 13%, similar to what we had measured when expressed alone in HEK293 cells (27). For Ch-SAP97-V puncta at synapses, the FRET efficiency was low, 5%, very similar to the values obtained for Ch-SAP97-V in HEK293 cells in puncta formed when coexpressed with CASK or NMDARs (27). The Ch-SAP97-V FRET efficiency outside of synapses indicates that a sizable pool of nonsynaptic SAP97 is mostly in the compact conformation, and is likely not associated with CASK or NMDARs, which associated with SAP97 in the extended conformation (27). At synapses, the Ch-SAP97-V FRET efficiency indicates that most, but not all, of SAP97 is in the extended conformation.

As a more direct measurement of PSD95 conformation, we used antibodies specific to mCherry (RFP) or Venus (YFP) to label the tags on Ch-PSD95-V expressed in cultured rat hippocampal neurons (Fig. 3*C*). We then used immuno-EM to measure the distance between the mCherry and Venus tags of Ch-PSD95-V in PSDs at spines, calculated from their individual distances to the postsynaptic membrane, and to visualize Ch-PSD95-V with EM tomography (Fig. 3 *C–F*). We found that immunogold labels with antibodies specific for N-terminal mCherry on PSD95 were located, on average, 18 nm from the postsynaptic membrane, whereas labels with antibodies specific for C-terminal Venus were located, on average, 28 nm away from the membrane (Fig. 3 *D* and *F*). The averaged ~10-nm separation between the PSD95 mCherry and Venus sites confirms the distance between the two fluorophores based on the FRET estimates for Ch-PSD95-V at synapses (Eq. **S2**). It is also consistent with PSD95 being oriented as a vertical filament, perpendicular to the plane of the postsynaptic membrane, with the palmitoylated N-terminal tag at the membrane and the C-terminal tag further away. This orientation was directly visualized when we performed EM tomography using immunogold labeling to the C-terminal Venus tag of Ch-PSD95-V in PSDs (Fig. 3*E*). Ch-PSD95-V appeared as a vertical filament perpendicular to the plane of the postsynaptic membrane with immunogold particles at the distal ends of the vertical filaments (1, 2).

We performed immunogold EM on tagged SAP97 to estimate the distance between the mCherry and Venus tags of Ch-SAP97-V in PSDs (Fig. 3 *C* and *D*). In contrast to what we observed with Ch-PSD95-V, there was no significant difference between the distance of the immunogold-labeled N-terminal mCherry tag and the C-terminal Venus tag from the postsynaptic membrane; both immunogold-labeled termini were, on average, 18 nm away from the membrane (Fig. 3 *C* and *D*) even though the FRET efficiency was essentially the

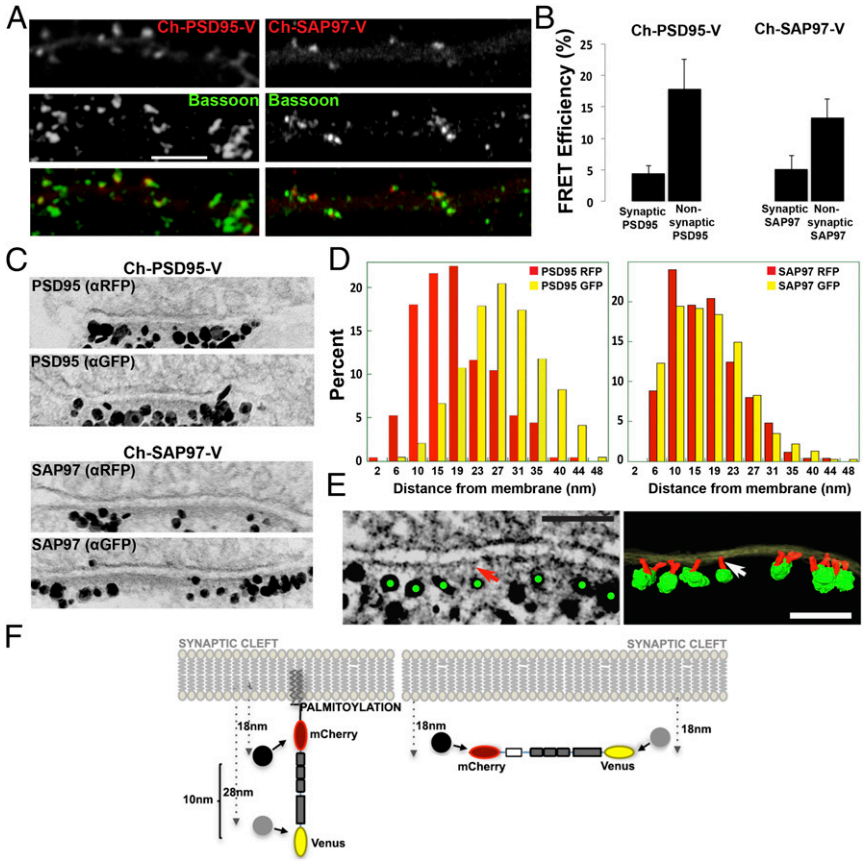


**Fig. 3.** Conformation and orientation of PSD95 and SAP97 at synapses. (*A*) Immunolocalization of Ch-PSD95-V and Ch-SAP97-V at synapses. Ch-PSD95-V (*Left*) or Ch-SAP97-V (*Right*) was transfected into cultured hippocampal neurons at 14 days in vitro (DIV). Displayed are dendrites immunolabeled with anti-Bassoon, a presynaptic marker, with Ch-PSD95-V or Ch-SAP97-V expression [FRET construct fluorescence (*Top*), anti-Bassoon (*Middle*), merged image (*Bottom*)]. (Scale bar: 5 μm.) (*B*) FRET efficiency values for Ch-PSD95-V (*Left*) and Ch-SAP97-V (*Right*) at synaptic and nonsynaptic regions. At synaptic sites, the FRET efficiency of Ch-PSD95-V was 4.5 ± 1.2%, and at nonsynaptic sites, it was 17.9 ± 4.6% (mean ± SEM; $n = 78$ puncta, 10 cells, $^*P < 0.01$). At synaptic sites, the FRET efficiency of Ch-SAP97-V was 5.2 ± 2.1%, and at nonsynaptic sites, it was 13.3 ± 2.9% (mean ± SEM; $n = 58$ puncta, 12 cells, $^*P < 0.02$). (*C*) Immuno-EM experiment measuring the distance of N and C termini of Ch-PSD95-V (*Top*) and Ch-SAP97-V (*Bottom*) from the PSD membrane. Representative EM images of synapses labeled separately with silver-enhanced immunogold particles against RFP (mCherry; *Top*) or GFP (Venus, *Bottom*) of Ch-PSD95-V and Ch-SAP97-V at the PSD. (*D*) Quantification of immuno-EM labeling measuring the distance between anti-RFP–labeled gold particles (red) and the membrane or anti-GFP gold particles (yellow) and membrane. For Ch-PSD95-V, distances were 18 ± 8 nm (mean ± SD; $n = 250$, 49 spines) for anti-RFP particles and 28 ± 8 nm ($n = 784$, 37 spines, $P < 0.0001$ by Student's *t* test) for anti-GFP particles. The measured distance between the N-terminal mCherry epitope and the C-terminal Venus epitope was therefore ~10 nm as summarized in *F*. For CH-SAP97-V, distances were 17 ± 7 nm (mean ± SD; $n = 250$, 35 spines) for anti-RFP particles and 18 ± 8 nm ($n = 377$, 26 spines, $P = 0.512$) for anti-GFP particles. There was no difference in the measured distance between the N-terminal mCherry and C-terminal Venus epitopes on Ch-SAP97-V. (*E*) EM tomography on Venus immunolabeled Ch-PSD95-V at PSD. (*Left*) Tomogram of the immunolabeling of Ch-PSD95-V against the C-terminal Venus site showing silver-enhanced immunogold particles (green dots) at the distal ends of vertical filaments (red arrow). (Scale bar: 100 nm.) (*Right*) Surface-rendered structural model based on the tomograms. Postsynaptic membrane (translucent yellow), PSD95 molecules as vertical filaments (red; indicated by white arrow), and enhanced immunogold particles (green) are shown. (Scale bar: 100 nm.) (*F*) Model of PSD95 and SAP97 orientation at the PSD. (*Left*) For Ch-PSD95-V, the average distance for the N terminus was 18 nm, and it was 28 nm for the C terminus (*D*), consistent with an orientation perpendicular to the PSD membrane. (*Right*) In contrast, there was no difference in the distance to the membrane between the N-terminal and C-terminal domains of SAP97 (*D*), consistent with an orientation parallel to the PSD membrane. The PSD95 extended conformation and orientation perpendicular to the PSD membrane was confirmed by EM tomography in *E* for Ch-PSD95-V, with anti-GFP sliver-enhanced gold particles in green and PSD95 in red.

same as the FRET efficiency of Ch-PSD95-V. This apparent inconsistency between the PSD95 and SAP97 can only be explained if SAP97 is in the extended conformation but oriented parallel to the plane of the postsynaptic membrane at the PSD (Fig. 3*F*).

**Increasing PSD95 Palmitoylation in PSDs Correlates with Increases in AMPAR but Not NMDAR Levels.** Because of our findings with HEK cells that palmitoylation regulates interactions with AMPARs and NMDARs (Fig. 2), we examined whether PSD95 palmitoylation regulates interactions with these receptors at cultured hippocampal neuronal synapses. The model in Fig. 4*A* is based on previous studies of PSD95 palmitoylation in neuronal cultures, which established that blockade of PSD95 palmitoylation with the inhibitor 2-BP (11, 23) reduced PSD95 and AMPAR levels but did not alter NMDAR levels at PSDs. Similar results were obtained by overexpressing C3,5S-PSD95, which cannot be palmitoylated (36). For PSD95 to be palmitoylated, it must interact with the PATs or DHHC proteins. DHHC2 is found primarily in dendrites or within PSDs (9, 23, 31). It palmitoylates PSD95 while in PSDs, and 2-BP acts largely by blocking DHHC2 in PSDs (23), allowing the unidentified PPT in PSDs to dominate and depalmitoylate PSD95 (23). As shown in the model, these findings also suggested that PSD95 depalmitoylation occurs at PSDs, and depalmitoylated PSD95 lacking its membrane anchor remains for some time in the PSD before exiting.

Based on our results using palmostatin B in HEK cells and increasing PSD95 palmitoylation (Fig. 1), we further tested the model (Fig. 4*A*) by treating hippocampal cultures with palmostatin B to

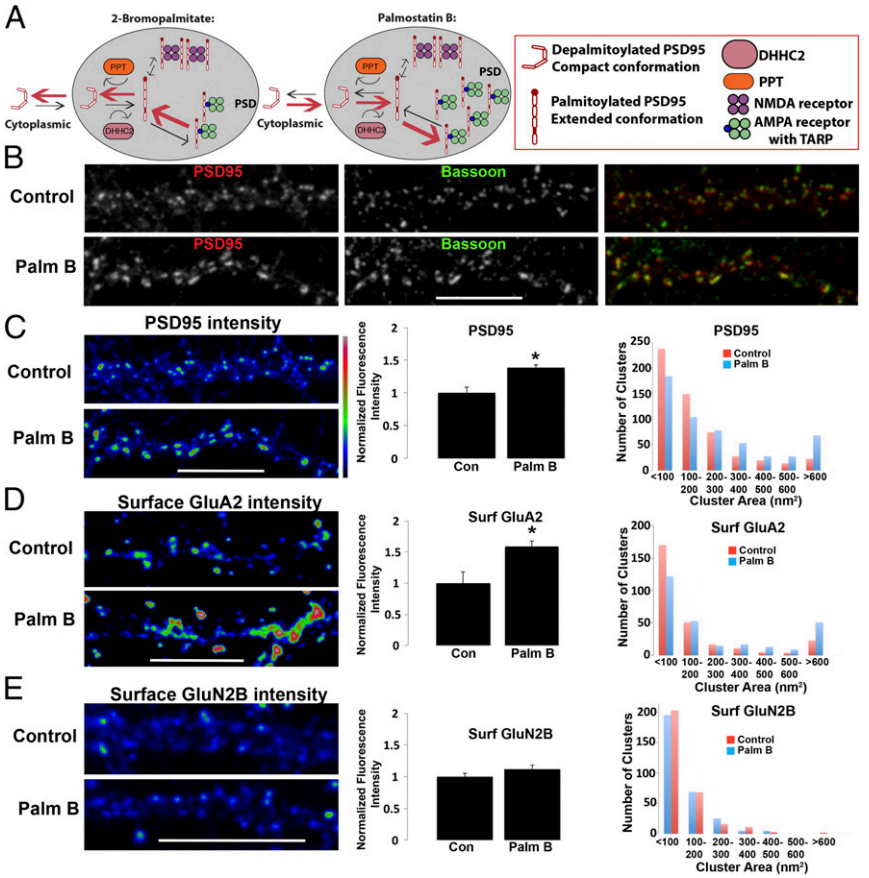


**Fig. 4.** Synaptic PSD95 and surface AMPARs increase with PSD95 palmitoylation. (*A*, *Left*) Summary model of previous results with 2-BP treatment of rat hippocampal neuronal cultures and how PSD95, AMPAR, and NMDAR levels were affected. (*A*, *Right*) Prediction of how palmostatin B blockade of PPT will affect PSD95, AMPAR, and NMDAR levels based on the model. (*B*) Control (*Top*) and palmostatin B-treated (*Bottom*) cultures (4 h) at DIV17 were coimmunolabeled with anti-PSD95 (*Left*) and anti-Bassoon, a presynaptic marker (*Center*) antibodies. Merged channel images are displayed (*Right*). (*C*, *Left*) Intensity profile of PSD95 fluorescence signal in *B*. (*C*, *Center*) Quantification of endogenous PSD95 pixel intensities on dendrites of untreated control and palmostatin B-treated cultures in *B*. Data are shown as mean ± SEM; control cells, 100 ± 8%; palmostatin B cells, 139 ± 5% ($n$ = 5–8 fields per group, $^*P < 0.02$ relative to control). (*C*, *Right*) Histogram showing the distribution of PSD95 punctal size (area) on control and palmostatin B-treated dendrites ($n$ = ∼545 puncta per group). (*D*, *Left*) Intact (nonpermeabilized) neurons (DIV17) were stained with an anti-GluA2 antibody to visualize surface AMPARs on control (*Top*) and palmostatin B-treated (*Bottom*) neurons. Displayed are intensity profiles of surface GluA2 fluorescence signal. (*D*, *Center*) Quantification of endogenous surface GluA2 staining on dendrites of untreated control and palmostatin B-treated cultures is shown. Data are shown as mean ± SEM; control cells, 100 ± 18%; palmostatin B cells, 159 ± 8% ($n$ = 6–10 fields per group, $^*P < 0.01$ relative to control). (*D*, *Right*) Histogram showing the distribution of surface GluA2 punctal size (area) on control and palmostatin B-treated dendrites ($n$ = ∼280 puncta per group). (*E*, *Left*) Intact (nonpermeabilized) neurons (DIV17) were stained with an anti-GluN2B antibody to visualize surface GluN2B-containing NMDARs on control (*Top*) and palmostatin B-treated (*Bottom*) neurons. Displayed are intensity profiles of surface GluN2B fluorescence signal. (*E*, *Center*) Quantification of endogenous surface GluN2B staining on dendrites of untreated control and palmostatin B-treated cultures. Data are shown as mean ± SEM; control cells, 100 ± 5%; palmostatin B cells, 112 ± 6% [$n$ = 8–10 fields per group, $P = 0.08$ (nonsignificant relative to control)]. (*E*, *Right*) Histogram showing the distribution of surface GluN2B punctal size (area) on control and palmostatin B-treated dendrites ($n$ = ∼300 puncta per group).

increase PSD95 palmitoylation in PSDs. We would expect, as shown in Fig. 4*A*, that palmostatin B should have the opposite effect of 2-BP with respect to PSD95 and receptor levels in PSDs. The levels of PSD95 (Fig. 4 *B* and *C*), cell-surface GluA2-containing AMPARs (Fig. 4*D*), and cell-surface GluN2B-containing NMDARs (Fig. 4*E*) were measured by immunostaining at spiny synapses. The staining intensities for each were measured for palmostatin B-treated and untreated conditions, as were the puncta size for each for the two conditions. As predicted in the model (Fig. 4*A*), the intensity and size of the puncta were significantly increased for PSD95 and AMPARs, but not for NMDARs. The trend toward a larger increase in levels observed for AMPARs compared with PSD95, although not significant, is predicted by the model because a portion of the PSD95 pool is bound to the NMDARs, and therefore is not changed with its palmitoylation. Thus, the results are consistent with the idea that when in PSDs, PSD95 is readily palmitoylated and depalmitoylated if associated with AMPARs, but in a more stable palmitoylated state if associated with NMDARs.

## Discussion

Because of the different roles AMPARs and NMDARs play in synaptic plasticity, a major question is how AMPAR and NMDAR dynamics are regulated by PSD scaffolding molecules. Here, we address this question by examining how palmitoylation regulates the conformation of a major PSD scaffolding molecule, PSD95, as well as its interactions with AMPARs and NMDARs. We previously found that SAP97 association with AMPARs and NMDARs is dictated by its conformation. An intramolecular SAP97 FRET sensor was used to demonstrate that SAP97 is in either an extended or compact conformation in vivo, and that SAP97 binds GluA1-containing AMPARs in the compact conformation and GluN2B-containing NMDARs in the extended conformation (27). SAP97 is normally in the compact conformation, but binding of the CASK

L27 domain to the SAP97 N-terminal L27 domain, or forming dimers of SAP97 through L27-L27 domain binding, changes SAP97 to an extended conformation. Thus, modification of the SAP97 N-terminal domain determines its conformation and whether it binds to AMPARs or NMDARs (27).

PSD95 is homologous to SAP97 except for its N-terminal domain, which has a palmitoylation site instead of an L27 domain. Using an intramolecular PSD95 FRET sensor, we demonstrate that, similar to SAP97, PSD95 is in either an extended or compact conformation in HEK cells, where PSD95 conformation is regulated by palmitoylation of the N-terminal domain. When palmitoylated, PSD95 is in the extended conformation; when depalmitoylated, it is in the compact conformation. Palmitoylated PSD95 binds GluN2B-containing NMDARs (Fig. 2*E*) like SAP97, but it also binds AMPARs through interactions with TARP subunits (Fig. 2*F*). These findings are consistent with a previous structural model based on EM tomography (1, 2, 37), where PSD95, as an extended filament, interacts with structures corresponding to NMDARs and AMPARs within PSDs.

Our results are relevant to understanding why there are different PSD-MAGUK isoforms and how they can compensate for each other in transgenic mouse knockouts (38–40). The nature of palmitoylation as a posttranslational modification explains, in part, the different orientations for PSD95 and SAP97 in PSDs. The PSD-MAGUK α-isoform splice variants of PSD95, SAP97, and PSD-93 all have N-terminal palmitoylation domains, and when palmitoylated, all would be anchored in the PSD membrane. Furthermore, palmitoylation would be expected to change their conformation from the compact to extended conformation as with PSD95 (Fig. 5*B*), resulting in the extended conformation perpendicular to the PSD membrane (Fig. 3*F*). The PSD-MAGUK β-isoform splice variants of PSD95, SAP97, and PSD-93 have an N-terminal L27 domain that replaces the palmitoylation domain. Lacking the ability to be palmitoylated, the β-isoform splice variants would not be expected to anchor their N termini to the plasma membrane. FRET data from the β-isoform of SAP97 in dissociated hippocampal neurons indicated that SAP97 exists as N termini-interacting dimers within PSDs (30). Intramolecular FRET data indicate that L27-L27–mediated SAP97 dimers are in the extended conformation, as opposed to a closed compact conformation (27). Altogether, it appears that SAP97 and the other PSD-MAGUK β-isoforms in PSDs are predominantly in the extended conformation as L27-L27–mediated, head-to-head dimers parallel to the plane of the membrane

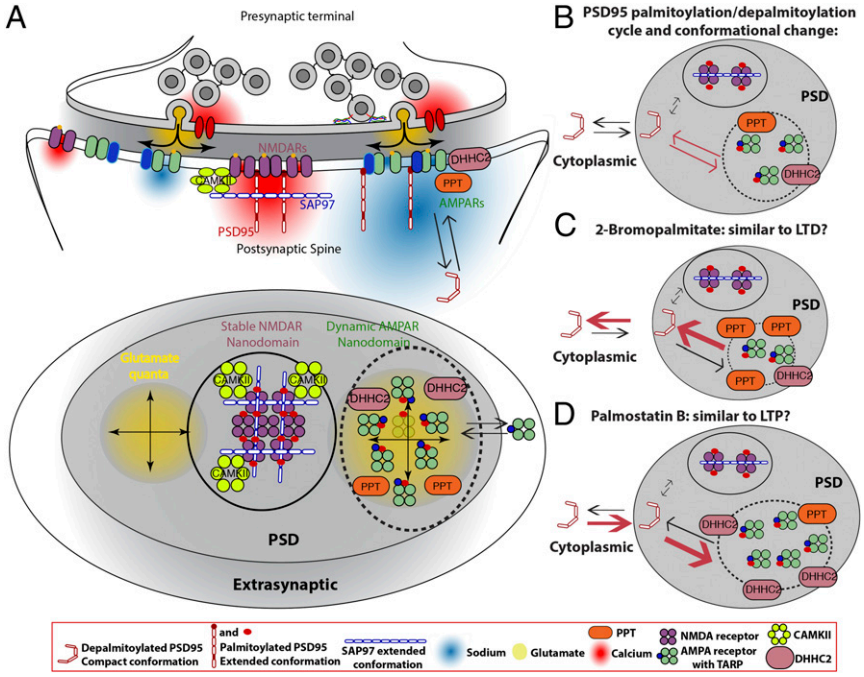


**Fig. 5.** Model of PSD95 and SAP97 scaffolding separate AMPAR and NMDAR nanodomains and how the PSD95 palmitoylation cycle regulates AMPAR dynamics in PSDs. Based on our results and the work of others, we propose that AMPARs and NMDARs in PSDs are differentially scaffolded into separate nanodomains (NMDAR nanodomain, circle; AMPAR nanodomain, dotted circle). In the NMDAR nanodomains, stronger PSD95–SAP97 interactions stabilize NMDARs and prevent access of palmitoylation/depalmitoylation enzymes, DHHC2 and PPT. The more dynamic AMPAR nanodomain results from weaker interactions between PSD95 and TARP-containing AMPARs, and allows access of palmitoylation/depalmitoylation enzymes. (*A*) Lateral (*Top*) and en face (*Bottom*) schematic views of the presynaptic domain synapsing on the PSD) of a spine head. In the model, we propose functional rationales for why AMPARs and NMDARs cluster in separate nanodomains in PSDs. First, separate nanodomains increase receptor packing density, and thereby increase the sodium current density for AMPARs (red cloud) and calcium current density for NMDARs (yellow). Second, separate nanodomains allow strategic positioning of the nanodomains. As shown, positioning of the AMPAR nanodomain with respect to the presynaptic vesicle release site will regulate the size of the AMPAR response, whereas positioning of the NMDAR nanodomain with respect to downstream calcium response proteins will regulate intracellular calcium signaling at the PSD. Finally, separate domains allow other proteins to segregate in either AMPAR or NMDAR nanodomains. An example is shown in *B–D* for the palmitoylation of PSD95. (*B–D*) Details of how the palmitoylation cycle changes PSD95 conformation and its association with AMPARs and NMDARs. (*B*) PSD95 in the compact conformation attaches to the PSD and is stabilized there in the extended conformation when palmitoylated. In this conformation, PSD95 associates mainly with AMPAR subunits containing TARP subunits, such as Stargazin, by entering AMPAR nanodomains or, occasionally, with GluN2B NMDAR subunits in NMDAR nanodomains. The subunits dissociate from PSD95 when depalmitoylation reverses PSD95 conformation, changing back to the compact conformation. In this way, the PSD95 palmitoylation/depalmitoylation cycle regulates the number of AMPAR slots in AMPAR nanodomains. (*C*) We propose that the number of AMPAR slots, and thus the levels of AMPARs and PSD95, are decreased by decreasing PSD95 palmitoylation by DHHC2 blockade with 2-BP incubation. (*D*) Number of AMPAR slots, as well as the levels of AMPARs and PSD95, is increased by increasing PSD95 palmitoylation by PPT blockade with palmostatin B incubation.

and that the L27-L27 interaction drives the conformational change from the compact to extended conformation. In this extended conformation, SAP97 interacts with NMDARs but not with AMPARs (27). Thus, in PSDs, we would expect that SAP97, and perhaps the other PSD-MAGUK β-isoforms, associate with NMDARs but not with AMPARs.

PSD95 palmitoylation is more dynamic when PSD95 is associated with AMPARs and more stable when it is associated with NMDARs (Fig. 4). What accounts for the changes in PSD95 palmitoylation when it interacts with AMPARs but not with NMDARs? Observations by superresolution light microscopy show palmitoylated PSD95 and AMPARs clustered in nanodomains (23). EM tomography suggested that the NMDAR nanodomains contained NMDAR–PSD95 complexes in 1:2 stoichiometry and that other PSD regions with AMPARs, but without NMDARs, contained extended PSD95–AMPAR complexes in a 1:1 stoichiometry (2). When PSD95 was acutely knocked down, AMPAR nanodomains were lost, whereas NMDAR nanodomains in PSDs were relatively preserved, consistent with the NMDAR nanodomains being more stable (1, 41). The presence of separate AMPAR and NMDAR domains in PSDs provides a simple explanation for why PSD95 palmitoylation and depalmitoylation are different at AMPARs and NMDARs. By segregating the palmitoyltransferase, DHHC2, and PPT very close to or within AMPAR nanodomains, and away from NMDAR nanodomains (Fig. 5), the PSD95 palmitoylation cycle would be dynamically driven in the AMPAR nanodomain but slower in the NMDAR nanodomain. As proposed (Fig. 5), palmitoylated and extended PSD95 in AMPAR nanodomains interacts with AMPARs through the AMPAR TARP PDZ-binding domain with a stoichiometry of 1:1. This stoichiometry could contribute to more dynamic AMPAR scaffolding in the AMPAR nanodomain. In NMDAR nanodomains, palmitoylated and extended PSD95 interacts with NMDARs through their GluN2B subunit PDZ-binding domain with a 2:1 stoichiometry. We propose that the higher stoichiometry of NMDAR–PSD95 interactions allows the dimeric, extended SAP97 to bind to NMDARs via interactions between SAP97 and PSD95, contributing to a lattice that serves to stabilize NMDAR within nanodomains separate from AMPAR nanodomains.

We propose that changes in PSD95 palmitoylation, depalmitoylation, and conformation occur independent of interaction with AMPARs or NMDARs (Fig. 5*B*). The alternative, that these processes occur while PSD95 is associated with the receptors, is also possible, but is not shown in the model. Supporting the notion that PSD95 and SAP97 both interact with NMDARs are the findings that PSD95 and SAP97 in brain homogenate can interact in a domain-specific manner (42) and that SAP97 is complexed with NMDARs (43). However, simultaneous PSD95, PSD93, and SAP102 knockdown in a SAP97 knockout mouse line did not further decrease NMDAR currents (44), suggesting that SAP97 associations with NMDARs in PSDs are not essential. Alternatively, without PSD95, PSD93, and SAP102, loss of SAP97 may have no effect because PSD95, PSD93, and/or SAP102 is required for SAP97–NMDAR interactions.

A number of functional advantages for clustering of AMPARs and NMDARs in separate nanodomains are apparent in the model displayed in Fig. 5. First, separate nanodomains increase the packing density of the receptors, and thereby increase the density of local sodium current at AMPARs and calcium current density at NMDARs. Second, separate nanodomains allow strategic positioning of receptors with respect to other synaptic domains, for instance, positioning clusters of NMDARs closer to or further away from intracellular, downstream, calcium-dependent effectors to regulate the effects of the intracellular calcium influx (45). Because of the lower affinity of AMPARs for glutamate (46), the positioning of AMPAR nanodomains close to or away from the glutamate release sites could regulate the level of AMPAR activation (21, 45). Increased AMPAR packing density, aligned with the presynaptic release sites, could significantly increase or decrease AMPAR synaptic currents without adding or subtracting AMPARs from the PSD. Third, different signaling molecules, as well as posttranslational modifying enzymes, could segregate with either AMPAR or NMDAR nanodomains, as shown for the palmitoylation enzymes in the AMPAR nanodomains and for CAMKII in the NMDAR nanodomains. Separation of modifying and signaling proteins could play a critical role in regulating trafficking in the PSD, so that the rate of AMPAR/NMDAR entry and exit, and other proteins into the domains, can be separately regulated, especially during plasticity events, such as long-term potentiation (LTP) and long-term depression (LTD). Evidence that separate PSD domains may have a role in synaptic plasticity includes the finding that treatment of cultures with 2-BP has an effect similar to LTD, whereas palmostatin B treatment has an effect similar to LTP (Fig. 5 *C* and *D*). Effects include the change in the size of the PSD with LTP and LTD, which we assume reflects the PSD95 cluster size (Fig. 4*C*), and changes in the ratio of the levels of AMPARs to NMDARs (Fig. 4 *D* and *E*).

## Experimental Procedures

**Culture of HEK293 Cells and Primary Hippocampal Neurons.** HEK293 cells were maintained in DMEM supplemented with 10% (vol/vol) calf serum (HyClone). Cells were transiently transfected with cDNA using a calcium phosphate protocol (47). Hippocampal cultures were prepared using neurobasal media, 2% (vol/vol) B27, and 2 mM L-glutamine. Briefly, hippocampi from embryonic day (E) 18 to E19 Sprague–Dawley rats were dissected and dissociated in 0.05% trypsin (vol/vol; Invitrogen), and cells were plated at a density of ~$4 \times 10^5$ cells per millimeter on polyethylenimine-coated, 12-mm coverslips. A detailed description of cell culture protocol and reagents is provided in *SI Experimental Procedures*.

**Electron Microscopy.** Transfection of 3-wk-old rat hippocampal cultures with FRET constructs using the Clontech CalPhos Mammalian Transfection Kit was followed by 40–44 h of incubation at 35 °C. For immuno-EM, these transfected neurons were fixed in 4% (vol/vol) paraformaldehyde in 0.1 M phosphate buffer at pH 7.4 for 45 min, Cultures were washed with buffer, permeabilized with 0.1% saponin, and blocked with 5% (vol/vol) normal goat serum in PBS for 1 h. They were then incubated with the primary antibody for 1 h, washed, incubated with the secondary antibody conjugated to 1.4-nm gold (Nanogold; Nanoprobes) for 1 h, washed again, and fixed with 2% (vol/vol) glutaraldehyde in PBS. Samples were silver-enhanced for 5–10 min (HQ Silver Enhancement Kit; Nanoprobes), treated with 0.2% osmium tetroxide in buffer for 30 min and then with 0.25% uranyl acetate overnight, washed, dehydrated in ethanol, and finally embedded in Epon. No specific labeling was present at PSDs when primary antibody was omitted from the protocol. Antibodies used were against mCherry, an RFP (rabbit polyclonal, 1:500; MBL), and against Venus, an YFP (mouse monoclonal, 1:500; Invitrogen). For immuno-EM, conventional thin EM sections were cut, grids were unselectively sampled, and images were collected of all synapses encountered in a JEOL-200CX transmission electron microscope with a bottom-mounted CCD camera (Advanced Microscopy Techniques Corp.). Immunogold particles in the immediate proximity of PSDs were analyzed, and the distance from the center of each particle to the postsynaptic membrane was measured with ImageJ (NIH). For EM tomography, sections 80 nm thick were mounted on Formvar-coated, 200-mesh, copper/nickel grids, and ~3 nm of carbon was evaporated to stabilize the grid. Gold particles (~10 nm) were applied to both sides of the grid as fiducial markers. Sections were scanned to identify spines for collecting dual-axis EM tomography series on an FEI Tecnai 300 kV transmission electron microscope with a field emission gun and bottom-mounted CCD camera at a dose of ~2,000 electrons per square nanometer per series. After the first series was acquired, the grid was rotated 90° and a second series was taken. Tilt increments were 2°, extending from +70° to −70°, and pixel sizes were 0.7 nm (2,048 × 2,048 image). Dual-axis image series were reconstructed by back-projection, and the 3D volume data were merged with IMOD (48). Fine alignment error was typically less than 0.2 pixel. The 3D volume data (tomogram) were analyzed and interpreted with EM3D (49), and segmented and surface-rendered with Amira (FEI). Segmentation, measurements, and surface rendering were performed as previously described (2, 37).

A detailed description of additional methods, reagents, imaging protocols, and calculation of FRET efficiencies is provided in *SI Experimental Procedures*.

**ACKNOWLEDGMENTS.** We thank Drs. Simon Alford and Nicolas Brunel for extensive discussions and help with the model proposed in Fig. 5 and Dr. Anitha Govind for her critical reading and helpful comments on the manuscript. We thank Drs. Vytas Bindokas and Paul Selvin for their technical support with FRET experiments. We also thank Drs. Christine Winters, Rita Azzam, Susan Cheng, and Virginia Crocker for help on immuno-EM and Drs. Alioscka Sousa and Richard Leapman for help on EM tomography data acquisition. This work was supported by the NIH under Grants NS043782, MH081251, and DA019695 (to W.N.G.) and by National Institute of Neurological Disorders and Stroke intramural funds (to T.S.R.). This project was also supported by the National Center for Research Resources and the National Center for Advancing Translational Sciences of the NIH through Grant UL1 RR024999 (to O.J.). The funders had no role in the study design, data collection and analysis, decision to publish, or preparation of the manuscript.

1. Chen X, et al. (2011) PSD-95 is required to sustain the molecular organization of the postsynaptic density. *J Neurosci* 31(17):6329–6338.
2. Chen X, et al. (2008) Organization of the core structure of the postsynaptic density. *Proc Natl Acad Sci USA* 105(11):4453–4458.
3. Xu W (2011) PSD-95-like membrane associated guanylate kinases (PSD-MAGUKs) and synaptic plasticity. *Curr Opin Neurobiol* 21(2):306–312.
4. Chen X, et al. (2005) Mass of the postsynaptic density and enumeration of three key molecules. *Proc Natl Acad Sci USA* 102(32):11551–11556.
5. Lowenthal MS, Markey SP, Dosemeci A (2015) Quantitative mass spectrometry measurements reveal stoichiometry of principal postsynaptic density proteins. *J Proteome Res* 14(6):2528–2538.
6. Chetkovich DM, et al. (2002) Postsynaptic targeting of alternative postsynaptic density-95 isoforms by distinct mechanisms. *J Neurosci* 22(15):6415–6425.
7. Elias GM, Nicoll RA (2007) Synaptic trafficking of glutamate receptors by MAGUK scaffolding proteins. *Trends Cell Biol* 17(7):343–352.
8. Lee S, Fan S, Makarova O, Straight S, Margolis B (2002) A novel and conserved protein-protein interaction domain of mammalian Lin-2/CASK binds and recruits SAP97 to the lateral surface of epithelia. *Mol Cell Biol* 22(6):1778–1791.
9. Noritake J, et al. (2009) Mobile DHHC palmitoylating enzyme mediates activity-sensitive synaptic targeting of PSD-95. *J Cell Biol* 186(1):147–160.
10. Craven SE, Bredt DS (2000) Synaptic targeting of the postsynaptic density protein PSD-95 mediated by a tyrosine-based trafficking signal. *J Biol Chem* 275(26):20045–20051.
11. El-Husseini Ael-D, et al. (2002) Synaptic strength regulated by palmitate cycling on PSD-95. *Cell* 108(6):849–863.
12. Kornau HC, Schenker LT, Kennedy MB, Seeburg PH (1995) Domain interaction between NMDA receptor subunits and the postsynaptic density protein PSD-95. *Science* 269(5231):1737–1740.
13. Niethammer M, Kim E, Sheng M (1996) Interaction between the C terminus of NMDA receptor subunits and multiple members of the PSD-95 family of membrane-associated guanylate kinases. *J Neurosci* 16(7):2157–2163.
14. Leonard AS, Davare MA, Horne MC, Garner CC, Hell JW (1998) SAP97 is associated with the alpha-amino-3-hydroxy-5-methylisoxazole-4-propionic acid receptor GluR1 subunit. *J Biol Chem* 273(31):19518–19524.
15. Dakoji S, Tomita S, Karimzadegan S, Nicoll RA, Bredt DS (2003) Interaction of transmembrane AMPA receptor regulatory proteins with multiple membrane associated guanylate kinases. *Neuropharmacology* 45(6):849–856.
16. Opazo P, Sainlos M, Choquet D (2012) Regulation of AMPA receptor surface diffusion by PSD-95 slots. *Curr Opin Neurobiol* 22(3):453–460.
17. Schnell E, et al. (2002) Direct interactions between PSD-95 and stargazin control synaptic AMPA receptor number. *Proc Natl Acad Sci USA* 99(21):13902–13907.
18. Bats C, Groc L, Choquet D (2007) The interaction between Stargazin and PSD-95 regulates AMPA receptor surface trafficking. *Neuron* 53(5):719–734.
19. Kharazia VN, Weinberg RJ (1997) Tangential synaptic distribution of NMDA and AMPA receptors in rat neocortex. *Neurosci Lett* 238(1-2):41–44.
20. Takumi Y, Ramírez-León V, Laake P, Rinvik E, Ottersen OP (1999) Different modes of expression of AMPA and NMDA receptors in hippocampal synapses. *Nat Neurosci* 2(7):618–624.
21. MacGillavry HD, Song Y, Raghavachari S, Blanpied TA (2013) Nanoscale scaffolding domains within the postsynaptic density concentrate synaptic AMPA receptors. *Neuron* 78(4):615–622.
22. Nair D, et al. (2013) Super-resolution imaging reveals that AMPA receptors inside synapses are dynamically organized in nanodomains regulated by PSD95. *J Neurosci* 33(32):13204–13224.
23. Fukata Y, et al. (2013) Local palmitoylation cycles define activity-regulated postsynaptic subdomains. *J Cell Biol* 202(1):145–161.
24. Lüscher C, et al. (1999) Role of AMPA receptor cycling in synaptic transmission and plasticity. *Neuron* 24(3):649–658.
25. Ehlers MD (2000) Reinsertion or degradation of AMPA receptors determined by activity-dependent endocytic sorting. *Neuron* 28(2):511–525.
26. Lin JW, et al. (2000) Distinct molecular mechanisms and divergent endocytotic pathways of AMPA receptor internalization. *Nat Neurosci* 3(12):1282–1290.
27. Lin EI, Jeyifous O, Green WN (2013) CASK regulates SAP97 conformation and its interactions with AMPA and NMDA receptors. *J Neurosci* 33(29):12067–12076.
28. Craven SE, El-Husseini AE, Bredt DS (1999) Synaptic targeting of the postsynaptic density protein PSD-95 mediated by lipid and protein motifs. *Neuron* 22(3):497–509.
29. Topinka JR, Bredt DS (1998) N-terminal palmitoylation of PSD-95 regulates association with cell membranes and interaction with K+ channel Kv1.4. *Neuron* 20(1):125–134.
30. Nakagawa T, et al. (2004) Quaternary structure, protein dynamics, and synaptic function of SAP97 controlled by L27 domain interactions. *Neuron* 44(3):453–467.
31. Fukata M, Fukata Y, Adesnik H, Nicoll RA, Bredt DS (2004) Identification of PSD-95 palmitoylating enzymes. *Neuron* 44(6):987–996.
32. Martin BR, Cravatt BF (2009) Large-scale profiling of protein palmitoylation in mammalian cells. *Nat Methods* 6(2):135–138.
33. Chen L, et al. (2000) Stargazin regulates synaptic targeting of AMPA receptors by two distinct mechanisms. *Nature* 408(6815):936–943.
34. Kim E, Sheng M (1996) Differential K+ channel clustering activity of PSD-95 and SAP97, two related membrane-associated putative guanylate kinases. *Neuropharmacology* 35(7):993–1000.
35. Dong YN, Waxman EA, Lynch DR (2004) Interactions of postsynaptic density-95 and the NMDA receptor 2 subunit control calpain-mediated cleavage of the NMDA receptor. *J Neurosci* 24(49):11035–11045.
36. El-Husseini AE, Schnell E, Chetkovich DM, Nicoll RA, Bredt DS (2000) PSD-95 involvement in maturation of excitatory synapses. *Science* 290(5495):1364–1368.
37. Chen X, et al. (2008) Identifying individual scaffolding molecules in the postsynaptic density. *Microsc Microanal* 14(Suppl 2):1068–1069.
38. Schlüter OM, Xu W, Malenka RC (2006) Alternative N-terminal domains of PSD-95 and SAP97 govern activity-dependent regulation of synaptic AMPA receptor function. *Neuron* 51(1):99–111.
39. Elias GM, Elias LA, Apostolides PF, Kriegstein AR, Nicoll RA (2008) Differential trafficking of AMPA and NMDA receptors by SAP102 and PSD-95 underlies synapse development. *Proc Natl Acad Sci USA* 105(52):20953–20958.
40. Elias GM, et al. (2006) Synapse-specific and developmentally regulated targeting of AMPA receptors by a family of MAGUK scaffolding proteins. *Neuron* 52(2):307–320.
41. Chen X, et al. (2015) PSD-95 family MAGUKs are essential for anchoring AMPA and NMDA receptor complexes at the postsynaptic density. *Proc Natl Acad Sci USA* 112(50):E6983–E6992.
42. Cai C, Li H, Rivera C, Keinänen K (2006) Interaction between SAP97 and PSD-95, two Maguk proteins involved in synaptic trafficking of AMPA receptors. *J Biol Chem* 281(7):4267–4273.
43. Frank RA, et al. (2016) NMDA receptors are selectively partitioned into complexes and supercomplexes during synapse maturation. *Nat Commun* 7:11264.
44. Levy JM, Chen X, Reese TS, Nicoll RA (2015) Synaptic consolidation normalizes AMPAR quantal size following MAGUK loss. *Neuron* 87(3):534–548.
45. Lisman J, Yasuda R, Raghavachari S (2012) Mechanisms of CaMKII action in long-term potentiation. *Nat Rev Neurosci* 13(3):169–182.
46. Clements JD, Lester RA, Tong G, Jahr CE, Westbrook GL (1992) The time course of glutamate in the synaptic cleft. *Science* 258(5087):1498–1501.
47. Claudio T (1992) Stable expression of heterologous multisubunit protein complexes established by calcium phosphate- or lipid-mediated cotransfection. *Methods Enzymol* 207:391–408.
48. Kremer JR, Mastronarde DN, McIntosh JR (1996) Computer visualization of three-dimensional image data using IMOD. *J Struct Biol* 116(1):71–76.
49. Harlow ML, Ress D, Stoschek A, Marshall RM, McMahan UJ (2001) The architecture of active zone material at the frog's neuromuscular junction. *Nature* 409(6819):479–484.
50. Ho SN, Hunt HD, Horton RM, Pullen JK, Pease LR (1989) Site-directed mutagenesis by overlap extension using the polymerase chain reaction. *Gene* 77(1):51–59.
51. Bresler T, et al. (2004) Postsynaptic density assembly is fundamentally different from presynaptic active zone assembly. *J Neurosci* 24(6):1507–1520.
52. Wu H, Reuver SM, Kuhlendahl S, Chung WJ, Garner CC (1998) Subcellular targeting and cytoskeletal attachment of SAP97 to the epithelial lateral membrane. *J Cell Sci* 111(Pt 16):2365–2376.
53. Kenworthy AK (2001) Imaging protein-protein interactions using fluorescence resonance energy transfer microscopy. *Methods* 24(3):289–296.
54. Drisdel RC, Green WN (2004) Labeling and quantifying sites of protein palmitoylation. *Biotechniques* 36(2):276–285.
55. Yap MC, et al. (2010) Rapid and selective detection of fatty acylated proteins using omega-alkynyl-fatty acids and click chemistry. *J Lipid Res* 51(6):1566–1580.